

Stochastic rocket dynamics under random nozzle side loads:
Ornstein-Uhlenbeck boundary layer separation and its coarse
grained connection to side loading and rocket response

R. G. Keanini*

Nilabh Srivastava[†]

Peter T. Tkacik[‡]

Department of Mechanical Engineering and Engineering Science

The University of North Carolina at Charlotte

Charlotte, North Carolina 28223-0001

David C. Weggel[§]

Department of Civil and Environmental Engineering

The University of North Carolina at Charlotte

Charlotte, North Carolina 28223-0001

P. Douglas Knight[¶]

Mitchell Aerospace and Engineering

Statesville, North Carolina 28677

Summary

A long-standing, though ill-understood problem in rocket dynamics, rocket response to random, altitude-dependent nozzle side-loads, is investigated. Side loads arise during low altitude flight due to random, asymmetric, shock-induced separation of in-nozzle boundary layers. In this paper, stochastic evolution of the in-nozzle boundary layer separation line, an essential feature underlying side load generation, is connected to random, altitude-dependent rotational and translational rocket response via a set of simple analytical models. Separation line motion, extant on a fast boundary layer time scale, is modeled as an Ornstein-Uhlenbeck process. Pitch and yaw responses, taking place on a long, rocket dynamics time scale, are shown to likewise evolve as OU processes. Stochastic, altitude-dependent rocket translational motion follows from linear, asymptotic versions of the full nonlinear equations of motion; the model is valid in the practical limit where random pitch, yaw, and roll rates all remain small. Computed altitude-dependent rotational and translational velocity and displacement statistics are compared against those obtained using recently reported high fidelity simulations [Srivastava, Tkacik, and Keanini, *J. Applied Phys.*, **108**, 044911 (2010)]; in every case, reasonable agreement is observed. As an important prelude, evidence indicating the physical consistency of the model introduced in the above article is first presented: it is shown that the study's separation line model allows direct *derivation* of experimentally observed side load amplitude and direction densities. Finally, it is found that the analytical models proposed in this paper allow straightforward identification of practical approaches for: i) reducing pitch/yaw response to side loads, and ii) enhancing pitch/yaw damping once side loads cease.

*Professor, Mechanical Engineering, 9201 University City Blvd., DCH 353; rkeanini@uncc.edu

†Assistant Professor, Mechanical Engineering, 9201 University City Blvd., DCH 355; nsrivast@uncc.edu

‡Assistant Professor, Mechanical Engineering, 9201 University City Blvd., DCH 354; ptkacik@uncc.edu

§Associate Professor, Civil Engineering, 9201 University City Blvd., Cameron 144; dcweggel@uncc.edu

¶Director, 500 West Broad Street, knight@mitchell.cc.nc.us

Key words: Ornstein-Uhlenbeck boundary layer separation, OU side load model, stochastic rocket dynamics, asymptotic rocket model

1. Introduction

Although the recorded history of powered rocket flight spans a millenium, dating to eleventh century China [1], and experimentally-based rocket development traces two hundred years to eighteenth century England [1], and while an enormous scientific and engineering literature attaches to the dynamics, design, and control of rockets, missiles, and spacecraft, numerous interesting, practically important questions remain. One of the most basic and well-studied concerns prediction of rocket trajectories during ascent. While the long time success of large rocket and missile programs suggests that this essential question has been solved, in fact, a variety of difficult-to-predict features introduce significant uncertainty. These include: i) altitude-, attitude-, and speed-dependent aerodynamic forces [2], ii) random loads produced by location- and altitude-dependent wind and atmospheric turbulence [3–6], iii) rocket design and construction imperfections [7], iv) fuel sloshing (liquid fuel rockets) [8, 9], v) slag formation (solid fuel rockets) [2], and vi) random impacts with air-borne animals and debris [10].

Random, nozzle side loads present a further, singularly ill-understood feature complicating ascent prediction. As depicted in Fig. 1, and as described, e.g., in [11, 12], nozzle side loads appear in over-expanded nozzles during low-altitude flight, when high ambient pressure forces external air upstream into the nozzle. Under these conditions, the inflow overcomes the low pressure, low inertia, near-wall nozzle out-flow. At a locus of points, the nominal, instantaneous boundary layer

separation line, inflow inertia decays sufficiently that outflow inertia can turn the inflow back on itself; the reversed inflow forms a virtual corner and, in turn, an oblique, circumferential shock. See Fig. 2.

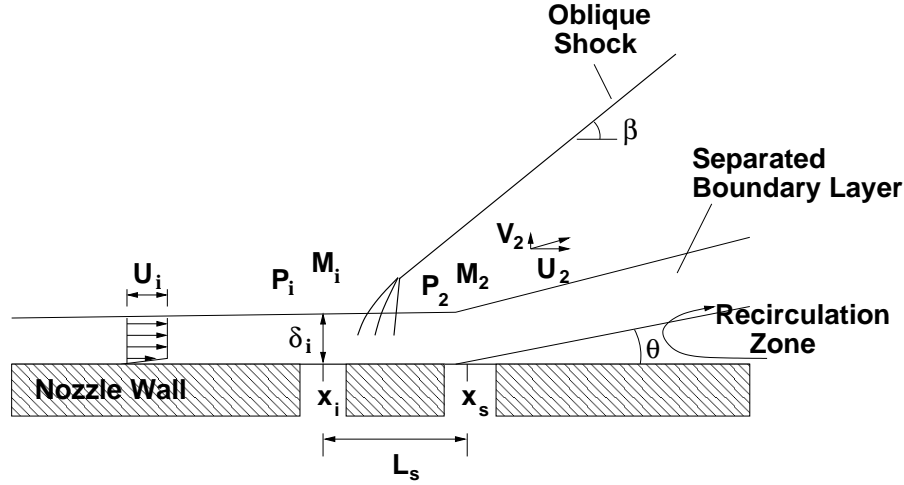


Figure 1: Shock-induced boundary layer separation in overexpanded supersonic nozzle flow. The process typically occurs during low altitude flight when ambient pressure is high enough to force atmospheric air into the nozzle. The incoming air flows upstream along the low-inertia, near-wall region until downstream-directed boundary layer inertia turns it, forming a virtual compression corner. An oblique shock thus forms, and the combined action of shock-induced pressure rise and inertial pressurization produced by the inflow forces the down-flow boundary layer to separate. Pressures, mach numbers, and velocities are denoted, respectively, by P , M , and U and V . Axial positions where the boundary layer starts to thicken (i denotes *incipient*), and where it separates are denoted, respectively, as x_i and x_s ; the nominal shock-boundary layer interaction zone is shown as L_s . Since the separation line position, x_s , and downstream conditions vary with the altitude-dependent ambient pressure, $P_a = P_a(H(t))$ [12], all variables shown likewise vary with $H(t)$.

Random side loads appear due to the pressure jump, ΔP , extant across the asymmetric, stochas-

tically evolving separation line. Viewing the instantaneous separation line as the superposition of the line's slowly moving mean axial position, $x_s(t)$, and it's rapid random fluctuation about $x_s(t)$, one observes that since $x_s(t)$ and ΔP are both altitude-dependent, random side loads, and resulting torques and translational and rotational rocket responses, are all likewise altitude-dependent.

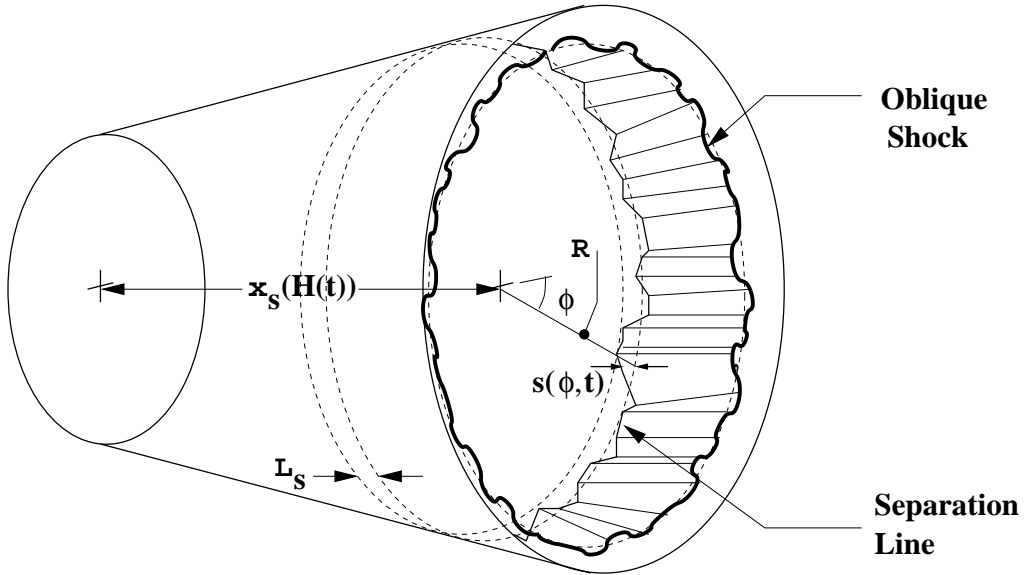


Figure 2: Schematic of stochastic boundary layer separation line and associated, rippled, azimuthal oblique shock. The mean separation line position relative to the nozzle throat, x_s , varies with rocket altitude, $H(t)$; the corresponding nozzle radius is $R = R(H(t))$. The instantaneous separation line position relative to $x_s(t)$ is shown as $s(\phi, t)$. The separation line lies on the nozzle wall and, in a nominally symmetric nozzle, the shock forms an azimuthally independent, average angle which varies with $x_s(t)$.

Supersonic flow separation and side load phenomena in nozzles, studied under fixed external pressure, i.e., effectively fixed altitude conditions, has attracted significant attention [13–22]; Ostlund and Muhammad-Klingmann [23] review much of this work. Numerical and experimental

studies have been reported, for example, by Frey and Hagemann [15, 24], Onofri and Nasuti [25], Pekkari [26], Schwane and Xia [27], and Shimizu et al. [28]. Fundamental studies of shock-boundary layer interactions [29–34] in which (typically oblique) shocks are produced by a variety of shock generators, have, in turn, provided essential insight into the fluid dynamic features underlying shock-induced separation.

Nozzle side loads can be perilous, damaging nozzles and/or attached equipment, or inducing catastrophic excitations within structural components; the failure of the Japanese H-II in 1999, for example, has been attributed to nozzle side loads [35]. In large engines, side load magnitudes can be extreme, on the order of 250,000 pounds, for example, in Saturn V engines [7]. Thus, minimizing and designing to accommodate side loading represents an essential rocket design task.

While side loads have long complicated ascent prediction, until recently [11], their effects on rocket dynamics have remained completely unknown. The work in [11] focused on the stochastic ascent of sounding-rocket-scale rockets subject to altitude-dependent random side loads and torques. A high fidelity numerical model was developed which incorporated the following features:

- a) a variable mass, six-degree-of-freedom, nonlinear rocket dynamics model [36],
- b) empirical models of the altitude-dependent ambient atmosphere [5] and mach number-dependent drag coefficient [37],
- c) a model of separation line motion which incorporated experimentally observed statistical properties of shock-separated flat plate turbulent boundary layers [31, 32, 34], and
- d) an *ad hoc*, though physically consistent model of side load statistics.

The model allowed Monte Carlo simulation of random rocket ascents, as well as estimates of altitude-dependent, ensemble-averaged translational and rotational velocities and displacements.

1.1. Objectives

Through the remainder of the paper, we will often refer collectively to the set of numerical models described in [11] as *Model I*; the present set of analytical models will likewise be referred to as *Model II*.

- A) The first, and most crucial objective centers on establishing the *physical consistency*, i.e., the congruence with physical principles and available experimental data, of both Models I and II. Due to the difficulties associated with detecting and isolating dynamic side loads within nozzles subject to simultaneous random aerodynamic and structural loading, obtaining experimental data on the effects of side loading on ascent will likely remain problematic. Indeed, no such data presently exists.

Thus, three key features motivate pursuit of this objective:

- i) substantial experimental challenges will likely continue to limit direct measurements,
- ii) theoretical insight is presently limited to the numerical models comprising Model I [11], and crucially,
- iii) demonstration of physical consistency establishes a reasonable foundation for further work on this long-standing problem.

The first objective is pursued in two steps.

- (a) We first show that the separation line model introduced in [11] allows *derivation* of both the *assumed* side load model in [11], as well as experimentally observed side load amplitude and direction densities [18–20]. See section 2.

Since Model I [11] incorporates a high fidelity rocket dynamics model and reasonable models of rocket aerodynamics and altitude-dependent ambient atmospheric conditions, and since the above demonstration ties the most uncertain portions of Model I, i.e., the separation line and side load models, to experimental observations [18–20], we argue that Model I [11] thus represents a physically consistent description of rocket ascent under altitude-dependent side loads.

- (b) Presuming the physical consistency of Model I [11], we then argue that since Model II predicts altitude-dependent rotational and translational rocket-response statistics that are, in every instance examined, consistent with those estimated via Model I (see section 7), Model II is likewise consistent.

B) It is found that the simple models comprising Model II provide a straightforward framework for interpreting observed random rocket responses to side loading, as well as for identifying practical approaches for designing against side loads. See section 7. The second objective thus centers on highlighting and exploiting this theoretical framework.

1.2. Overview

The following models and interconnecting elements tie stochastic separation line motion to rocket response, and thus comprise the paper’s essential frame:

- i) Local, short-time-scale separation line dynamics are modeled as an Ornstein-Uhlenbeck process. (See section 3.) Here, as depicted in Fig. 2, *local* refers to axial separation line motion in the vicinity of any given in-nozzle azimuthal angle, ϕ , while the short time scale corresponds to the correlation time for local axial separation line displacements. We will sometimes refer to the latter as the *boundary layer time scale*.
- ii) Since side load evolution takes place on this short time scale, while rocket response to side loading occurs on a much longer time scale, it becomes necessary to derive a coarse grained time correlation function for local separation line displacement appropriate to the longer scale. This procedure in turn leads to the crucially important (long-time-scale) side load time correlation function. See section 4.
- iii) Given the latter, and focusing first on rocket rotational dynamics, we show in section 5 that the stochastic evolution of pitch and yaw likewise correspond to Ornstein-Uhlenbeck processes. Once this key result is obtained, then theoretical expressions for altitude-dependent means and variances of the pitch and yaw rate and pitch and yaw displacement follow. Additionally, and as becomes apparent when interpreting results in section 7, parametric relationships obtained for associated (effective) damping and diffusion coefficients provide practical guidance for minimizing the effects of side loads on rotational dynamics.
- iv) An asymptotic model of translational rocket motion, appropriate in the practical limit where pitch, yaw, and roll all undergo small random variations about zero, follows in section 6. Again, the simplified linear model, derived from the general nonlinear model in [11], allows analytical determination of altitude-dependent means and variances for the rocket's lateral

velocity and displacement components.

Once a complete model is thus established, altitude-dependent variances of pitch and yaw rate, pitch and yaw displacement, lateral velocities, and lateral displacements are computed and compared against ensemble average estimates obtained via the model in [11] (section 7).

2. Physical consistency of Model I

As detailed in [11], and in response to the decaying altitude-dependent ambient pressure, the mean position of boundary layer separation line, $x_s(t)$, travels down the nozzle axis toward the nozzle exit, with motion taking place on a relatively slow time scale, $\tau_a = \Delta x_a / V_R$, where Δx_a is the characteristic incremental altitude over which ambient pressure varies and V_R is the characteristic rocket speed. Superposed on this slow motion is a fast, random, azimuthally homogeneous stochastic motion. Following [11], the joint probability density, p_s , associated with the instantaneous random separation line shape is given by

$$p_s(s_1, s_2, \dots, s_N) = \prod_I p_I = \frac{1}{(2\pi\sigma_s^2)^{N/2}} \exp \left[-\frac{s_1^2 + s_2^2 + s_3^2 + \dots + s_N^2}{2\sigma_s^2} \right] \quad (1)$$

where, as shown in Fig. 3, s_I is the random axial displacement of the separation line at azimuthal angle ϕ_I , and σ_s^2 is the (assumed) constant variance of local separation line displacements.

Constituent displacements in the set of N displacements are assumed independent, and based

on experimental observations [31,32,34], gaussian. Thus, each p_I is given by

$$p_I(s_I) = \frac{1}{\sqrt{2\pi\sigma_s^2}} \exp \left[-\frac{s_I^2}{2\sigma_s^2} \right] \quad (2)$$

In moving to a continuous description of the separation line, [11] assumes that

$$\langle s(\phi, t)s(\phi', t) \rangle = \sigma_s^2 \delta(\phi - \phi') \quad (3)$$

Considering next the side load, we express the instantaneous force vector produced by asymmetric boundary layer separation, $\mathbf{F}_s(t)$, as a sum of radial and axial components

$$\mathbf{F}_s(t) = \mathbf{F}_r(t) + \mathbf{F}_x(t) \quad (4)$$

In [11], the following *ad hoc* side load model was assumed:

A) F_{sy} and F_{sz} are independent, gaussian random variables,

B) $\langle F_{sy} \rangle = 0$ and $\langle F_{sz} \rangle = 0$,

C) $\langle (F_{sy} - \langle F_{sy} \rangle)^2 \rangle = \langle (F_{sz} - \langle F_{sz} \rangle)^2 \rangle = \sigma^2$,

where, assuming ergodicity, $\langle \cdot \rangle$ denotes either an ensemble or time average, and where the separation line model above is used to calculate the force variance σ^2 . The side load components F_{sy} and F_{sz} are expressed with respect to rocket-fixed coordinates; see Fig. 4 in section 5 below.

In order to demonstrate the physical consistency of Model I, we first show that the *assumed* properties, A) -C), can be *derived* from the simple separation line model in [11]. We then follow [11]

and show that the model in A) - C) leads to experimentally observed side load amplitude and direction densities.

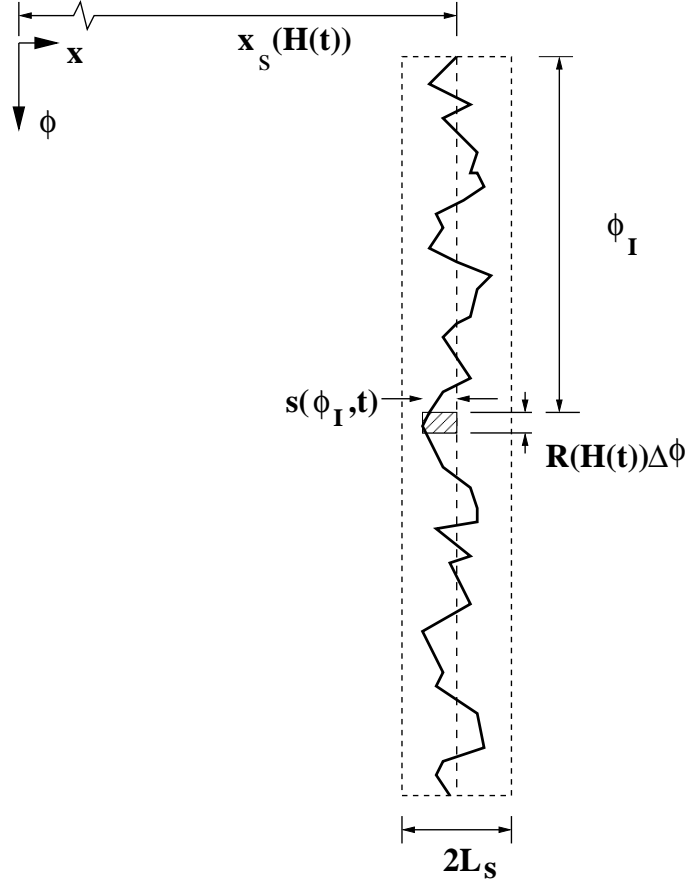


Figure 3: Model I [11] separation line model. The mean separation line position, $x_s(H(t))$, moves down the nozzle axis, on the slow time scale associated with vertical rocket motion. By contrast, axial separation line motion about $x_s(H(t))$, at any angular position, ϕ_I , is random, and takes place on a much shorter time scale. Rapid axial motion, in addition, is confined to the nominal shock-boundary layer interaction zone, again denoted by L_s . Pressures upstream and downstream of the instantaneous separation line, $P_i = P_i(H(t))$ and $P_2 = P_2(H(t))$, respectively, are assumed to be spatially uniform within L_s . Adapted from [11].

Considering assumption B) first, we calculate:

$$\langle F_{sy}(H(t)) \rangle_s = R[H(t)] [P_i(H(t)) - P_a(H(t))] \int_0^{2\pi} \sin \phi \langle s(\phi, t) \rangle_s d\phi \quad (5)$$

and

$$\langle F_{sz}(H(t)) \rangle_s = R[H(t)] [P_i(H(t)) - P_a(H(t))] \int_0^{2\pi} \cos \phi \langle s(\phi, t) \rangle_s d\phi \quad (6)$$

where $R(H(t))$ is the nozzle radius at the axial location of the mean separation line at time t , $P_i(H(t)) - P_a(H(t)) = \Delta P(H(t))$, is the pressure jump across the separation-inducing shock at altitude $H(t)$, P_i and P_a are the wall pressures immediately upstream and downstream of the instantaneous separation line, and where we have approximated the downstream pressure as the instantaneous ambient pressure, $P_a(H(t))$ [3,8,15]. See [11] for further discussion.

In order to evaluate these averages, express the k^{th} realization of, e.g., F_{sz} , in discrete form as

$$F_{sz}^{(k)}(s_1, s_2, \dots, s_N) = R[H(t)] [P_i(H(t)) - P_a(H(t))] \sum_{I=1}^M s^{(k)}(\phi_I) \cos \phi_I \Delta \phi \quad (7)$$

where $s^{(k)}(\phi_I)$ is the associated separation line displacement at ϕ_I . Taking the ensemble average term by term, and noting that

$$\langle s_I \rangle_s = \int_{-\infty}^{\infty} \int_{-\infty}^{\infty} \dots \int_{-\infty}^{\infty} s_I p_s(s_1, s_2, \dots, s_N) ds_1 ds_2 \dots ds_N = 0$$

then confirms B):

$$\langle F_{sy}(H) \rangle_s = 0 \quad \langle F_{sz}(H) \rangle_s = 0 \quad (8)$$

Turning next to A), since F_{sy} and F_{sz} represent sums of say, N independent gaussian random variables, then both are gaussian. Computing

$$\langle F_{sy}(H)F_{sz}(H) \rangle = R^2(H)\Delta P^2(H)\sigma_s^2 \int_0^{2\pi} \frac{1}{2} \sin 2\phi d\phi = 0$$

where (3) has been used, likewise shows that $F_{sy}(H)$ and $F_{sz}(H)$ are independent.

Finally, for C), since $\langle F_{sy}^2(H) \rangle = R^2(H)\Delta P^2(H)\sigma_s^2 \int_0^{2\pi} \cos^2 \phi d\phi$, and $\langle F_{sz}^2(H) \rangle = R^2(H)\Delta P^2(H)\sigma_s^2 \int_0^{2\pi} \sin^2 \phi d\phi$, then

$$\langle F_{sy}^2(H) \rangle = \langle F_{sz}^2(H) \rangle \quad (9)$$

2.1. Derivation of density functions for side load amplitude and direction

We note two important experimental and numerical observations concerning the side load, \mathbf{F}_s (within rigid, axisymmetric nozzles):

- a) the probability density of the random amplitude, $A = |\mathbf{F}_s|$, is a Rayleigh distribution [18–20],
and
- b) the random instantaneous direction, ϕ_s , of \mathbf{F}_s is uniformly distributed over the periphery of the nozzle, or $p_{\phi_s}(\phi_s) = 1/2\pi$, where p_{ϕ_s} is the pdf of the side load direction [18–20].

As noted, both observations can be *derived*, starting from the simple statistical model of random side loads, A) - C), immediately above. Thus, given A and ϕ_s , the instantaneous side load

components in body-fixed y and z directions (see Fig. 4) are given by

$$F_{sy} = A \cos \phi_s \quad F_{sz} = A \sin \phi_s$$

Following [11], write F_{sy} and F_{sz} as $F_{sy} = \bar{Y} = A \cos \phi_s$ and $F_{sz} = \bar{Z} = A \sin \phi_s$; thus, the joint probability density associated with F_{sy} and F_{sz} can be expressed as

$$p_{\bar{Y}\bar{Z}}(\bar{Y}, \bar{Z}) = p_{\bar{Y}}(\bar{Y})p_{\bar{Z}}(\bar{Z}) = \frac{1}{2\pi\sigma^2} \exp\left(-\frac{\bar{Y}^2 + \bar{Z}^2}{2\sigma^2}\right) \quad (10)$$

Following [11], we restate $p_{\bar{Y}\bar{Z}}$ in terms of A and ϕ_s as,

$$p_{A\phi_s} = |J|p_{\bar{Y}\bar{Z}}(\bar{Y}, \bar{Z}) \quad (11)$$

where $p_{A\phi_s}(A, \phi_s)$ is the joint pdf for the random amplitude and direction of \mathbf{F}_r , and where the jacobian determinant is given by

$$|J| = \begin{vmatrix} \frac{\partial \bar{Y}}{\partial A} & \frac{\partial \bar{Y}}{\partial \phi_s} \\ \frac{\partial \bar{Z}}{\partial A} & \frac{\partial \bar{Z}}{\partial \phi_s} \end{vmatrix} = A \quad (12)$$

Thus,

$$p_{A\phi_s}(A, \phi_s) = \frac{A}{2\pi\sigma^2} \exp\left(-\frac{A^2}{2\sigma^2}\right) = \left(\frac{1}{2\pi}\right) \left[\frac{A}{\sigma^2} \exp\left(-\frac{A^2}{2\sigma^2}\right)\right] = p_{\phi_s}(\phi_s)p_A(A) \quad (13)$$

where,

$$p_{\phi_s}(\phi_s) = \frac{1}{2\pi} \quad 0 < \phi_s \leq 2\pi \quad (14)$$

is the uniform probability density underlying the random direction ϕ_s , and

$$p_A(A) = \frac{A}{\sigma^2} \exp\left(-\frac{A^2}{2\sigma^2}\right) \quad (15)$$

is the Rayleigh distribution for the amplitude A .

In summary, we have shown that the separation line model in [11]: i) allows derivation of the assumed side load model, A) - C), in [11], and ii) provides a theoretical basis for explaining experimentally observed [18–20] side load amplitude and direction densities.

3. Ornstein-Uhlenbeck model of separation line dynamics

Theoretical determination of rocket response to side loads requires that the time correlation function for either side load component, $\langle F_{s\alpha}(t')F_{s\alpha}(t) \rangle$, be first determined. This and the next section develops $\langle F_{s\alpha}(t')F_{s\alpha}(t) \rangle$ in two steps. First, we propose (and physically justify) that local separation line dynamics can be modeled as an Ornstein-Uhlenbeck process. Once this assumption is made, then the second step rests on a rigorous argument showing that on the relatively long rocket dynamics time scale, the boundary layer separation line shape, and importantly, associated side load components, are all delta correlated in time. See section 4.

We propose the following simple, explicit stochastic model of separation line dynamics:

$$ds_i(t) = -ks_i(t) + \sqrt{D_s}dW(t) \quad (16)$$

where $s_i(t) = s(\phi_i, t)$ is the instantaneous separation line position at ϕ_i , k and D_s are damping and effective diffusion coefficients, and $dW(t)$ is a differential Wiener process. This equation, describing an Ornstein-Uhlenbeck process, allows straightforward, physically consistent calculation of statistical properties associated with separation line motion and, more importantly, serves as the first link in a chain that connects short-time-scale random separation line motion to short-time-scale random side loads, and in turn, to long-time-scale stochastic rotational rocket dynamics.

The form of this equation is chosen based on the following experimental features, observed in shock-separated flows near compression corners and blunt fins:

- a) Under statistically stationary conditions, the feet of separation-inducing shocks oscillate randomly, up- and downstream, over limited distances, about a fixed mean position; see, e.g., [31, 32, 34].
- b) As observed in [32, 34] the distribution of shock foot positions within the shock-boundary layer interaction zone is approximately gaussian.
- c) The time correlation of shock foot positions, as indicated by wall pressure measurements within the shock-boundary layer interaction zone, decays rapidly for time intervals, Δt , larger than a short correlation time, τ_s , a feature that can be inferred, for example, from [38].

Physically, the damping term captures the fact that the shock sits within a pressure-potential

energy well. Thus, downstream shock excursions incrementally decrease and increase, respectively, upstream and downstream shock face pressures; the resulting pressure imbalance forces the shock back upstream. A similar mechanism operates during upstream excursions. Introduction of a Weiner process models the combined random forcing produced by advection of turbulent boundary layer structures through the upstream side of the shock foot and pressure oscillations emanating from the downstream separated boundary layer and recirculation zone.

We note that the proposed model is qualitatively consistent with Plotkin's model of boundary layer-driven shock motion near compression corners and blunt fins [38]. Plotkin's model, which captures low frequency spectra of wall pressure fluctuations within these flows, corresponds to a generalized Ornstein-Uhlenbeck process in which a deterministic linear damping term is superposed with a non-Markovian random forcing term. We use an ordinary OU process model, incorporating a Wiener process, since again, it is consistent with the above observations and more particularly, since it allows much simpler calculation of statistical properties.

4. Derivation of the coarse grained side load time correlation function

Given the model in Eq. (16), our path shifts to obtaining a mathematically consistent description of resulting side load statistics. To accomplish this, we take advantage of the significant separation in time scales that exists between large-scale, low frequency random separation line motion [31,32,34], and the relatively slow dynamics of the rocket. Thus, define the long time scale as $\tilde{t} = t \epsilon^{-1}$, where $\epsilon \ll 1$ is a dimensionless scale factor and t is the (short) time scale associated with low frequency,

large scale separation line motion. The long time scale can be chosen to correspond to any of a number of dynamical features; the chosen scale determines ϵ . Since we are interested in the dynamical response of the rocket, we choose \tilde{t} to be on the order of $\tau_R = LV_R^{-1}$, where L and V_R are the length and characteristic speed of the rocket. Thus, $\epsilon = f^{-1}\tau_R^{-1}$, where f is a characteristic frequency from the low frequency band associated with large scale shock foot motion [31,32]. Based on the rocket parameters given in [11], τ_R is on the order of $2(10^{-2})$ s; thus, since f^{-1} is on the order of 10^{-3} s [32,34], $\epsilon = O(10^{-2})$ to $O(10^{-1})$.

Using well known expressions [39] for the mean and variance of an OU process, one can readily show that the process becomes stationary on time scales that are long relative to the characteristic period for large scale separation line motion, i.e., for $t \gg k^{-1}$. Under stationary conditions, the variance becomes independent of time, $var(s_i(t)) = D_s / (2k)$, and the time correlation can be placed in the form:

$$\langle s_i(\tau) s_i(0) \rangle_s = \frac{D_s \tau_c}{2} \exp(-|\tau| / \tau_c) \quad (17)$$

where $\tau = t_2 - t_1$, and $\tau_c = \int_0^\infty \langle s_i(t) s_i(0) \rangle dt / var(s_i(t))$, is the correlation time. Under stationary conditions, $\tau_c = k^{-1}$ and $var(s_i(t)) = D_s \tau_c / 2 = \sigma_s^2$.

Given the above time correlation, we can now show that on long time scales, \tilde{t} , $\langle s_i(\tau) s_i(0) \rangle_s$, approaches delta-function like character. First, define a normalized time correlation function as

$$R_s(\tau) = \frac{\langle s_i(\tau) s_i(0) \rangle_s}{2\sigma_s^2 \tau_c} \quad (18)$$

where $\int_{-\infty}^{\infty} R_s(\tau) d\tau = 1$. Next, define a rescaled version of $R_s(\tau)$ as $R_{s\epsilon}(\tilde{\tau}) = \epsilon^{-1} R_s(\epsilon^{-1}\tau)$, or

$$R_{s\epsilon}(\tilde{\tau}) = \frac{\langle s_i(\tilde{\tau}) s_i(0) \rangle_s}{2\sigma_s^2 \tau_c \epsilon} \quad (19)$$

where $\tilde{\tau} = \epsilon^{-1}\tau$. Finally, for small ϵ , $R_{s\epsilon}(\tilde{\tau}) \rightarrow \delta(\tilde{\tau})$. Thus, since $\epsilon \ll 1$, the long-time-scale behavior of the time correlation function can be stated as

$$\langle s_i(\tilde{\tau}) s_i(0) \rangle_s = 2\sigma_s^2 \tau_c \epsilon \delta(\tilde{\tau}) \quad (20)$$

Thus, from this point on, we focus on time scales that are on the order of the rocket-dynamics time scale, τ_R , drop the tilde on \tilde{t} , and specify

$$\langle s(\varphi', t') s(\varphi, t) \rangle_s = 2\sigma_s^2 \tau_c \epsilon \delta(\varphi' - \varphi) \delta(t' - t) \quad (21)$$

as the long-time-scale space-time correlation for $s(\varphi, t)$, where again we assume delta correlated statistics in the angular direction [11].

Given this correlation, the long-time-scale time correlations for the side load components can be finally calculated by combining and averaging instantaneous, non-averaged versions of Eqs. (5) and (6):

$$\langle F_{sy}(t') F_{sy}(t) \rangle_s = \langle F_{sz}(t') F_{sz}(t) \rangle_s = R(t') R(t) \triangle P(t') \triangle P(t) 2\pi \sigma_s^2 \tau_c \epsilon \delta(t' - t) \quad (22)$$

Obtaining the long-time-scale side load time correlation function represents a crucial step since

it allows calculation of side load effects on rocket rotational and translational dynamics.

5. Pitch and yaw rate response to random side loading

Given $\langle F_{sy}(t')F_{sy}(t) \rangle = \langle F_{sz}(t')F_{sz}(t) \rangle$, derived above, we now show that during the period when side loads act, $0 < t \leq T$, the long-time-scale evolution of the rocket's pitch and yaw rates correspond to Ornstein-Uhlenbeck processes. Given this key result, altitude-dependent means and variances for the rocket's pitch and yaw rates, both during the side load period and after, can be determined.

5.1. Derivation of Ornstein-Uhlenbeck rotational dynamics

As a necessary point of reference, we first note the equations governing rotational dynamics [11]:

$$I_{xx}\dot{\omega}_x + \left(\dot{I}_{xx} + \frac{2}{5}|\dot{M}|R_e^2 \right) \omega_x = 0 \quad (23)$$

$$I\dot{\omega}_y + (I_{xx} - I)\omega_x\omega_z + \dot{I}\omega_y + |\dot{M}|[(L - b)^2 + 0.25R_e^2]\omega_y - \frac{|\dot{M}|LR_R^4}{10v_eR_e^2}\omega_x\omega_z = \mathbf{M}_{ext} \cdot \mathbf{j} \quad (24)$$

$$I\dot{\omega}_z - (I_{xx} - I)\omega_x\omega_y + \dot{I}\omega_z + |\dot{M}|[(L - b)^2 + 0.25R_e^2]\omega_z + \frac{|\dot{M}|LR_R^4}{10v_eR_e^2}\omega_x\omega_y = \mathbf{M}_{ext} \cdot \mathbf{k} \quad (25)$$

Regarding notation, moments of inertia are evaluated with respect to rocket- fixed coordinates, $I = I(t)$ and $I_{xx} = I_{xx}(t)$ are, respectively, the moments of inertia with respect to either lateral coordinate, z or y , and the longitudinal rocket axis, R_R , L , b , and R_e , are, respectively, rocket radius, rocket length and half-length, and nozzle exit radius, v_e is the speed of the exiting flow from the nozzle, \dot{M} is the associated mass flux, and ω_x , ω_y , and ω_z are, respectively, the roll, yaw, and

pitch rates. Unit vectors $\mathbf{i}, \mathbf{j}, \mathbf{k}$, are those of the rocket-fixed system. See [11] for a full description and Fig. 4 for a schematic of the rotational and translational variables describing rocket motion.

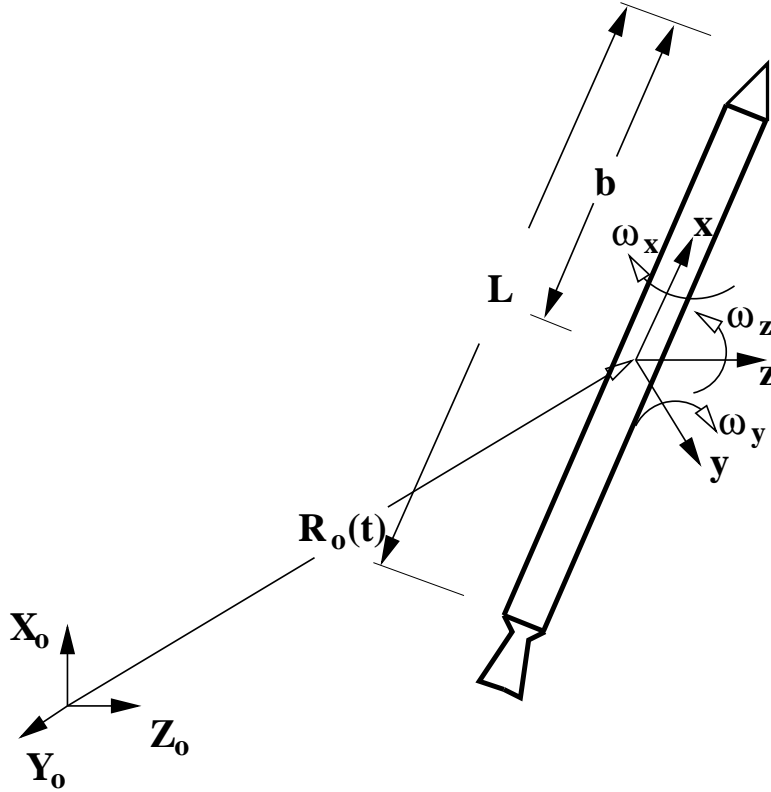


Figure 4: Rocket model. Roll, pitch, and yaw rates are shown, respectively, as ω_x , ω_z , and ω_y ; center of mass position is given by $R_o(t) = [X_o(t), Y_o(t), Z_o(t)]$, while rocket-fixed coordinates are $[x, y, z]$. See [11] for further details.

Since the line of action of the aerodynamic load is assumed coincident with the rocket's longi-

tudinal axis, the only force that contributes to the external moment, \mathbf{M}_{ext} , in Eqs. (24) and (25) is the in-nozzle stochastic side load. The moment due to these stochastic side loads can thus be computed as

$$\mathbf{M}_{ext} = -(L - b + x_s(t))\mathbf{i}_x (F_{sy}\mathbf{j} + F_{sz}\mathbf{k}) \quad (26)$$

As an important aside, and as a means of isolating side load effects, the present model, as well as that in [11], does not incorporate wind loading. A simple scaling argument (see Appendix B) indicates that random winds: i) under most conditions, do not excite rotational motion, and ii) simply function as an *additive* source of variance in the rocket's *translational* motion. In other words, wind appears to have minimal influence on the stochastic, altitude-dependent evolution of *rotational* dynamics. Rather, (launch-site-specific) mean and random winds simply produce whole-rocket, random, *lateral translational* motion, superposed on a deterministic translational drift.

During the short side load period, and as found by scaling, it is observed from the equation governing roll, Eq. (23), that the coefficients on $\dot{\omega}_x$ and ω_x , I_{xx} and $(\dot{I} + \frac{2}{5}|\dot{M}|R_e^2)$, respectively, remain essentially constant. [As shown in [11], for the model considered, the side load period, T , is approximately 10.85 s.] Thus, for an assumed initial roll rate, $\omega_x(0) = 0$, and during the side load period, $0 \leq t \leq T$, the rate of roll remains zero, $\omega_x = 0$. Indeed, as shown in [11], and due to the absence of roll-inducing torques, this feature holds throughout any given simulated flight.

Thus, we focus on the evolution of yaw and pitch, as determined by Eqs. (24) and (25), respectively, and observe that these can be placed in the forms:

$$d\omega_y = -A(t)\omega_y(t)dt + B(t)F_{sz}(t)dt \quad (27)$$

$$d\omega_z = -A(t)\omega_z(t)dt - B(t)F_{sy}(t)dt \quad (28)$$

where

$$A(t) = [\dot{I} + |\dot{M}|[(L-b)^2 + 0.25R_e^2] / I \quad (29)$$

is a positive damping coefficient (positive as determined by a straightforward order of magnitude analysis) and

$$B(t) = (L-b) / I(t)$$

Next, from, e.g., [39], we note that gaussian, zero mean random functions that are delta correlated in time, such as $F_{sz}(t)$ and $F_{sy}(t)$, can be related to Wiener processes via

$$B(t)F_{sz}(t)dt = \sqrt{D(t)}dW_z(t) = \sqrt{D(t)}[W_z(t+dt) - W_z(t)] \quad (30)$$

where $W_z(t)$ is a Wiener process associated with $F_{sz}(t)$, $D(t)$ is a diffusion coefficient, and where a similar expression holds for $F_{sy}(t)$. Here, using

$$\iint_t^{t+\Delta t} B(t'')B(t') < F_{sz}(t'')F_{sz}(t') >_s dt''dt' = \iint_t^{t+\Delta t} \sqrt{D(t'')}\sqrt{D(t')}dW_z(t'')dW_z(t') = D(t)\Delta t \quad (31)$$

it is readily shown that

$$D(t) = (L-b)^2 I^{-2}(t) R^2(t) \Delta^2 P(t) 2\pi\sigma_s^2 \tau_c \varepsilon \quad (32)$$

where, consistent with dimensional requirements, $D(t)$ has units of t^{-3} .

Thus, we arrive at the important result that during the period $0 \leq t \leq T$, the random rotational dynamics of the rocket correspond to Ornstein-Uhlenbeck processes:

$$d\omega_y = -A(t)\omega_y(t)dt + \sqrt{D(t)}dW_z(t) \quad (33)$$

$$d\omega_z = -A(t)\omega_z(t)dt - \sqrt{D(t)}dW_y(t) \quad (34)$$

We discuss in section 7 the physical features underlying the competition between damping, as embodied by the terms involving $A(t)$ in (33) and (34), and amplification of pitch and yaw rates, as captured by the $D(t)$ terms.

5.2. Pitch and yaw rate response

While in many problems, the damping and diffusion coefficients are constant, here they are not. Nevertheless, Eqs. (33) and (34) can be integrated (for individual realizations) via an integrating factor:

$$\omega_\alpha(t) = \exp\left(-\int_0^t A(s') ds'\right) \int_0^t \left\{ \sqrt{D(s')} \exp\left(\int_0^{s'} A(s'') ds''\right) \right\} dW(s') \quad (35)$$

where the subscript α denotes either y or z . Given Eq. (35), the mean yaw and pitch rates can be determined:

$$\langle \omega_\alpha(t) \rangle = \exp\left(-\int_0^t A(s') ds'\right) \int_0^t \left\{ \sqrt{D(s')} \exp\left(\int_0^{s'} A(s'') ds''\right) \right\} \langle dW(s') \rangle$$

or since $\langle dW(s') \rangle = 0$,

$$\langle \omega_\alpha(t) \rangle = 0 \quad 0 \leq t < T \quad (36)$$

[Note, we are abusing standard notation by expressing the expectation over Wiener processes, $E_{\omega,s'} W(s' + ds') - W(s')$ as $\langle dW(s') \rangle$.] Likewise, (35) allows determination of the time-dependent variances for pitch and yaw rates:

$$\begin{aligned} \langle \omega_\alpha^2(t) \rangle &= \exp\left(-2 \int_0^t A(s') ds'\right) \int_0^t \int_0^t \left\{ \sqrt{D(s')D(p')} \exp\left(\int_0^{s'} A(s'') ds''\right) \exp\left(\int_0^{p'} A(p'') dp''\right) \right\} \langle d\beta_{s'p'} \rangle \\ &= \int_0^t \int_0^t \{F(s', p')\} \langle dW(s') dW(p') \rangle \end{aligned}$$

where $\langle d\beta_{s'p'} \rangle = \langle dW(s') dW(p') \rangle$. Expressing the term $\int_0^t \int_0^t \{F(s', p')\} \langle dW(s') dW(p') \rangle$ as a discrete double sum and using $\Delta W_i \Delta W_j = \Delta t \delta_{ij}$, it is readily shown that

$$\langle \omega_\alpha^2(t) \rangle = \exp\left(-2 \int_0^t A(s') ds'\right) \int_0^t \left\{ D(s') \exp\left(2 \int_0^{s'} A(s'') ds''\right) \right\} ds' \quad 0 \leq t < T \quad (37)$$

It is also easily shown that in the case of constant A and D , this formula leads to the well-known [39] variance expression for constant coefficient OU processes.

During the post-side load period, $T \leq t \leq T_f$, the (short-time-scale) side load terms in equations (27) and (28) no longer appear, and thus neither do associated (long-time-scale) Wiener processes in Eqs. (33) and (34). Thus, carrying out a single realization integration of the latter two equations,

we obtain

$$\omega_{\alpha}(t) = \omega_{\alpha}(T) \exp \left[- \int_T^t A(q) dq \right] \quad (38)$$

where $\omega_{\alpha}(T)$ is a random initial condition on the post-side load pitch and yaw rate evolution equations. Since $\langle \omega_{\alpha}(T) \rangle = 0$, it is clear that

$$\langle \omega_{\alpha}(t) \rangle = 0 \quad T < t \leq T_f \quad (39)$$

consistent with numerical results in [11].

Likewise, forming $\langle \omega_{\alpha}^2(t) \rangle$ and using

$$\langle \omega_{\alpha}^2(T) \rangle = \exp \left(-2 \int_0^T A(s') ds' \right) \int_0^T \left\{ \exp \left(2 \int_0^{s'} A(s'') ds'' \right) \right\} ds' \quad (40)$$

obtained from Eq. (37), the time-dependent variance of yaw and pitch rates during the post-side-load period follow as:

$$\langle \omega_{\alpha}^2(t) \rangle = \langle \omega_{\alpha}^2(T) \rangle \exp \left[-2 \int_T^t A(q) dq \right] \quad T < t \leq T_f \quad (41)$$

In closing this subsection, we again note that the rocket's rate of roll, ω_x , is uncoupled from moments produced by random side loads (see Eq. (23)); this is reflected in the solution of Eq. (23):

$$\omega_x(t) = \omega_x(0) \exp \left[\int_0^t F(t') dt' \right] \quad (42)$$

where $F(t') = [\dot{I}_{xx} + \frac{2}{5}|\dot{M}|R_e^2]\dot{I}_{xx}^{-1}$. Thus, for an assumed initial roll rate of zero, roll rate remains zero, $\omega_x(t) = 0$, throughout any given flight. Again, computed results in [11] are consistent with this observation.

5.3. Pitch and yaw angle response

Here, time-dependent pitch and yaw angle variances are determined, as well as the time correlation function, $\langle \psi_\alpha(t')\psi_\alpha(t) \rangle$, where ψ_α represents either the pitch or yaw angle. Determining the evolution of pitch/yaw variances provides a further consistency check between theory and numerical experiments, and, in addition, provides important physical insight into the large, almost explosive growth in translational velocity and displacement variances described in section 6 below. The time correlation function is needed in order to determine these lateral translational responses.

During the side load period, single realization evolution of pitch and yaw angles follows by integration of (35):

$$\psi_\alpha(t) = \int_0^t \exp f(q) G_\alpha(q) dq \quad (43)$$

where

$$f(q) = - \int_0^q A(q'') dq'' \quad (44)$$

and

$$G_\alpha(q) = - \int_0^q \left[\sqrt{D(s')} \exp \int_0^{s'} A(s'') ds'' \right] dW_\alpha(s') \quad (45)$$

Taking the expectation over the Weiner process, $dW_\alpha(s')$, we find, consistent with numerical

experiments, that mean pitch and yaw angles remain fixed at zero throughout the side load period:

$$\langle \psi_\alpha(t) \rangle = 0 \quad 0 \leq t < T \quad (46)$$

Evolution of pitch/yaw angle variance during $0 \leq t < T$ is given by

$$\langle \psi_\alpha^2(t) \rangle = \int_0^t \int_0^t \exp f(q') \exp f(q) \langle G_\alpha(q') G_\alpha(q) \rangle dq' dq \quad (47)$$

or, using

$$\begin{aligned} \left\langle \int_0^{t_1} F(s') dW(s') \cdot \int_0^{t_2} F(s'') dW(s'') \right\rangle &= \int_0^{\min(t_1, t_2)} F^2(s') ds', \\ \langle \psi_\alpha^2(t) \rangle &= \int_0^t \int_0^t \exp f(q') \exp f(q) \left(\int_0^{\min(q, q')} D(s') \left[\exp 2 \int_0^{s'} 2A(s'') ds'' \right] ds' \right) dq' dq \end{aligned} \quad (48)$$

which, by symmetry, becomes:

$$\langle \psi_\alpha^2(t) \rangle = 2 \int_0^t \left[\int_0^{q'} \exp f(q') \exp f(q) \left(\int_0^q D(s') \left[\exp 2 \int_0^{s'} 2A(s'') ds'' \right] ds' \right) dq \right] dq' \quad (49)$$

The detailed form of (49) appropriate to the present rocket model is given in Appendix A.

Following the side load period, pitch/yaw evolution follows by integration of (38):

$$\psi_\alpha(t) = \omega_\alpha(T) \int_T^t h(s') ds' + \psi_\alpha(T) \quad (50)$$

where

$$h(s') = \exp \left(- \int_T^{s'} A(s'') ds'' \right) \quad (51)$$

Taking the expectation again shows that average pitch/yaw angles remain at zero throughout the post-side-load period:

$$\langle \psi_\alpha(t) \rangle = 0 \quad T \leq t \leq T_f \quad (52)$$

where, by (35), $\langle \omega_\alpha(T) \rangle = 0$. Again, this is consistent with results of numerical experiments in [11].

Post-side-load variance follows directly from (50):

$$\begin{aligned} \langle \psi_\alpha^2(t) \rangle = & \langle \omega_\alpha^2(T) \rangle \left(\int_T^t h(s') ds' \right)^2 + 2 \langle \omega_\alpha(T) \psi_\alpha(T) \rangle \left(\int_T^t h(s') ds' \right) + \\ & + \langle \psi_\alpha^2(T) \rangle \quad T \leq t \leq T_f \end{aligned} \quad (53)$$

where the correlation $\langle \omega_\alpha(T) \psi_\alpha(T) \rangle$ is non-zero and is given by

$$\langle \omega_\alpha(T) \psi_\alpha(T) \rangle = \int_0^T \exp f(q) \exp f(T) \langle G_\alpha(q) G_\alpha(T) \rangle dq \quad (54)$$

or

$$\langle \omega_\alpha(T) \psi_\alpha(T) \rangle = \int_0^T \int_0^q \int_0^T \exp f(q) \exp f(T) \sqrt{D(s')} \sqrt{D(s'')} g(s') g(s'') \langle dW_\alpha(s') dW_\alpha(s'') \rangle dq \quad (55)$$

or finally by

$$\langle \omega_\alpha(T) \psi_\alpha(T) \rangle = \int_0^T \exp f(q) \exp f(T) \int_0^q D(s') g^2(s') ds' dq \quad T \leq t \leq T_f \quad (56)$$

Here, $g(s') = \exp \left(\int_0^{s'} A(p) dp \right)$, and f and G_α are given, respectively, by (44) and (45). The

detailed problem-specific form of (56) is again given in Appendix A.

6. Asymptotic rocket response to small- amplitude stochastic pitch and yaw

Under conditions where the rocket experiences zero-mean stochastic side loading, we anticipate that the Euler angles $\phi(t)$, $\theta(t)$, and $\psi(t)$ all undergo small, random variations about zero. Under these conditions, a leading order asymptotic model of rocket lateral velocity and displacement response can be used to validate and interpret the numerically estimated statistics obtained via Model I.

Thus, considering the full translational equations of motion given in [11], we observe that under conditions where

$$[\phi(t), \theta(t), \psi(t)] = O(\epsilon_o) \quad (57)$$

for all t , where $\epsilon_o \ll 1$, these equations assume the forms:

$$M\ddot{X}_o = (P_e - P_a)A_e + |\dot{M}|v_e - 0.5C_DA_R\rho_a(\dot{X}_o^2 + \dot{Y}_o^2 + \dot{Z}_o^2) - Mg + O(\epsilon_o) \quad (58)$$

$$M\ddot{Y}_o = F_T\psi + F_{sy} + 2|\dot{M}|(L - b)\omega_z + O(\epsilon_o) \quad (59)$$

$$M\ddot{Z}_o = F_T\theta + F_{sz} - 2|\dot{M}|(L - b)\omega_y + O(\epsilon_o) \quad (60)$$

where

$$F_T = (P_e - P_a)A_e + |\dot{M}|v_{ex}$$

is the total thrust force, and where $\phi(t)$, $\theta(t)$, and $\psi(t)$ correspond, respectively, to roll, pitch, and yaw angles. Other new terms include the rocket mass, $M = M(t)$, the nozzle exit pressure and exit area, P_e and A_e , the (mach number dependent) drag coefficient, C_D , the rocket cross-sectional area, A_R , the altitude-dependent ambient density, ρ_e , and the rocket center-of-mass position $[X_o(t), Y_o(t), Z_o(t)]$. See Fig. 4, and refer to [11] for a detailed description.

An important note: scaling, as well as results below show that the thrust terms (involving F_T) in the lateral equations of motion, (59) and (60), must be included; due to the magnitude of F_T , even small, order ϵ pitch and yaws can produce non-negligible, and indeed, dominant lateral forces. In addition, due to the restriction of $\phi(t)$ to small magnitudes, the following development does not hold when the rocket is given a non-zero roll. Note too another abuse of notation in the use of dimensional terms in the order symbols.

Due to the importance of minimizing random lateral velocities and displacements, and due to the miniscule effects of side loads on vertical motion [11], we focus on rocket dynamics in the lateral (i.e., y - and z -) directions. The above equations show that during the side load period, $0 \leq t < T$, leading order lateral translational dynamics are determined by the summed effects of three random forces:

- a) the nozzle side load, $F_{s\eta}$,
- b) the lateral thrust component, $\pm F_T \psi_{\alpha\pm}$, produced by random variations in pitch and yaw angles, and
- c) a second reaction term, $\pm 2|\dot{M}|(L-b)\omega_{\alpha\pm}$, produced by incremental (random) changes in the direction of the mass flux vector, $\dot{\mathbf{M}}$.

[Here, $\psi_{\alpha+} = \psi$, the yaw angle, $\psi_{\alpha-} = \theta$, the pitch angle, $\omega_{\alpha+} = \omega_z$, the pitch rate, and $\omega_{\alpha-} = \omega_y$, the yaw rate.] Following the side load period, only the latter two random forcing terms continue to act.

Letting $\eta(t)$ represent either $Y_o(t)$ or $Z_o(t)$, and focusing in turn on the side load and post-side-load periods, one can integrate equations (59) and (60) to obtain single realization solutions. Thus, over the side load period,

$$\dot{\eta}(t) = \int_0^t \frac{F_{s\eta}(s')}{M(s')} ds' \pm 2(L-b) \int_0^t \frac{|\dot{M}(s')|}{M(s')} \omega_{\alpha\pm}(s') ds' \pm \int_0^t \frac{F_T(s')\psi_{\alpha\pm}(s')}{M(s')} ds' \quad 0 \leq t < T \quad (61)$$

while over the post-side-load period

$$\dot{\eta}(t) = \dot{\eta}(T) \pm 2(L-b) \int_T^t \frac{|\dot{M}(s')|}{M(s')} \omega_{\alpha\pm}(s') ds' \pm \int_T^t \frac{F_T(s')\psi_{\alpha\pm}(s')}{M(s')} ds' \quad T \leq t \leq T_f \quad (62)$$

[Use Eqs. (59) and (60) to choose the signs in (61) and (62).]

In order to determine single realization displacements, first define

$$G_\eta(t) = \int_0^t \frac{F_{s\eta}(s')}{M(s')} ds' \quad (63)$$

$$H_\eta(t; t_o) = 2(L-b) \int_{t_o}^t \frac{|\dot{M}(s')|}{M(s')} \omega_{\alpha\pm}(s') ds' \quad (64)$$

$$\tilde{F}(t; t_o) = \int_{t_o}^t \frac{F_T(s')\psi_{\alpha\pm}(s')}{M(s')} ds' \quad (65)$$

and integrate (61) and (62) to obtain:

$$\eta(t) = \int_0^t G_\eta(s') ds' \pm \int_0^t H_\eta(s'; 0) ds' \pm \int_0^t \tilde{F}(s'; 0) ds' \quad 0 \leq t < T \quad (66)$$

$$\eta(t) = \dot{\eta}(T)(t - T) \pm \int_T^t H_\eta(s'; T) ds' \pm \int_T^t \tilde{F}(s'; T) ds' \quad T \leq t < T_f \quad (67)$$

Given Eqs. (61) and (62), time-dependent ensemble average lateral velocities are readily calculated:

$$\langle \dot{\eta}(t) \rangle = \int_0^t \frac{\langle F_{s\eta}(s') \rangle}{M(s')} ds' \pm 2(L - b) \int_0^t \frac{|\dot{M}(s')|}{M(s')} \langle \omega_{\alpha\pm}(s') \rangle ds' \pm \int_0^t \frac{F_T(s') \langle \psi_{\alpha\pm}(s') \rangle}{M(s')} ds' \quad 0 \leq t < T$$

$$\langle \dot{\eta}(t) \rangle = \langle \dot{\eta}(T) \rangle \pm 2(L - b) \int_T^t \frac{|\dot{M}(s')|}{M(s')} \langle \omega_{\alpha\pm}(s') \rangle ds' \pm \int_T^t \frac{F_T(s') \langle \psi_{\alpha\pm}(s') \rangle}{M(s')} ds' \quad T \leq t \leq T_f$$

From Eqs. (8), (36) and (39), it is clear that ensemble average lateral velocity components remain zero throughout the entire flight period:

$$\langle \dot{\eta}(t) \rangle = 0 \quad 0 \leq t \leq T_f \quad (68)$$

a result that is again consistent with numerical experiments [11].

Variances of the lateral velocity components likewise follow from Eqs. (61) and (62):

$$\begin{aligned}
\langle \dot{\eta}^2(t) \rangle = & \int_0^t \int_0^t \left\langle \frac{F_{s\eta}(s')}{M(s')} \frac{F_{s\eta}(p')}{M(p')} \right\rangle ds' dp' + 4(L-b)^2 \int_0^t \int_0^t \frac{|\dot{M}(s')|}{M(s')} \frac{|\dot{M}(p')|}{M(p')} \langle \omega_{\alpha\pm}(s') \omega_{\alpha\pm}(p') \rangle ds' dp' + \\
& + \int_0^t \int_0^t \frac{F_T(s') F_T(p')}{M(s') M(p')} \langle \psi_{\alpha\pm}(s') \psi_{\alpha\pm}(p') \rangle ds' dp' + \\
& + 2(L-b) \int_0^t \int_0^t \frac{|\dot{M}(s')|}{M(s')} \frac{F_T(p')}{M(p')} \langle \psi_{\alpha\pm}(p') \omega_{\alpha\pm}(s') \rangle ds' dp' \quad (69)
\end{aligned}$$

for $0 \leq t < T$, and where it is assumed that pitch and yaw rates are uncorrelated with side loads,

$$\langle \omega_{\alpha\pm}(s') F_{s\alpha}(p') \rangle = 0.$$

Similarly, over the post-side-load period, $T \leq t \leq T_f$,

$$\begin{aligned}
\langle \dot{\eta}^2(t) \rangle = & \langle \dot{\eta}^2(T) \rangle + 4(L-b)^2 \int_T^t \int_T^t \frac{|\dot{M}(s')|}{M(s')} \frac{|\dot{M}(p')|}{M(p')} \langle \omega_{\alpha\pm}(s') \omega_{\alpha\pm}(p') \rangle ds' dp' + \\
& + \int_T^t \int_T^t \frac{F_T(s') F_T(p')}{M(s') M(p')} \langle \psi_{\alpha\pm}(s') \psi_{\alpha\pm}(p') \rangle ds' dp' + \\
& + 2(L-b) \int_T^t \int_T^t \frac{|\dot{M}(s')|}{M(s')} \frac{F_T(p')}{M(p')} \langle \psi_{\alpha\pm}(p') \omega_{\alpha\pm}(s') \rangle ds' dp' \quad (70)
\end{aligned}$$

where we assume that $\langle \dot{\eta}(T) \int_T^t \frac{|\dot{M}(s')|}{M(s')} \omega_{\alpha\pm}(s') ds' \rangle = 0$. See Appendix A for problem-specific versions of (69) and (70).

Ensemble averages and variances for lateral displacements can be obtained using the single realization solutions in Eqs. (66) and (67). Thus, it is again readily shown that average lateral displacements are zero both during and after the side-loading period:

$$\langle \eta(t) \rangle = \int_0^t \langle G_\eta(s') \rangle ds' \pm \int_0^t \langle H_\eta(s'; 0) \rangle ds' \pm \int_0^t \tilde{F}(s') ds' = 0 \quad 0 \leq t < T \quad (71)$$

$$\langle \eta(t) \rangle = \langle \dot{\eta}(T) \rangle (t - T) \pm \int_T^t \langle H_\eta(s'; T) \rangle ds' \pm \int_T^t \tilde{F}(s') ds' = 0 \quad T \leq t < T_f \quad (72)$$

which is again consistent with [11]. Note, G_η , H_η , and \tilde{F} are given by Eqs. (63), (64) and (65), respectively.

Variances are likewise found:

$$\begin{aligned} \langle \eta^2(t) \rangle = & \int_0^t \int_0^t \langle G_\eta(s') G_\eta(p') \rangle ds' dp' + \int_0^t \int_0^t \langle H_\eta(s'; 0) H_\eta(p'; 0) \rangle ds' dp' + \\ & + \int_0^t \int_0^t \langle \tilde{F}(s'; 0) \tilde{F}(p'; 0) \rangle ds' dp' \quad 0 \leq t < T \end{aligned} \quad (73)$$

$$\begin{aligned} \langle \eta^2(t) \rangle = & \langle \dot{\eta}^2(T) \rangle (t - T)^2 + \int_T^t \int_T^t \langle H_\eta(s'; T) H_\eta(p'; T) \rangle ds' dp' + \\ & + \int_T^t \int_T^t \langle \tilde{F}(s'; T) \tilde{F}(p'; T) \rangle ds' dp' \quad T \leq t < T_f \end{aligned} \quad (74)$$

where it is assumed that all cross-correlations between G_η , H_η , \tilde{F} , and $\eta(T)$ are zero. Problem-specific versions of (73) and (74) are given in Appendix A.

7. Results and discussion

As an important preliminary, we list essential explanatory remarks and observations.

- A) As shown in Appendix A, most working variance formulae involve one or more time-dependent terms: $\Delta P(t)$, $R(t)$, $M(t)$, and $I(t)$. Here, these (non-stochastic) terms are determined using numerical data from execution of Model I [11]. In cases where the current model (Model II) is used to predict the dynamics of actual rockets, $R(t)$, the time-dependent nozzle radius

corresponding to the instantaneous mean separation line position, $x_s(t)$, represents the most difficult-to-determine parameter. At least two straightforward approaches, i.e., methods not requiring high-level modeling and computation, are available. The first [12], combines one of several semi-empirical separation pressure correlations, see, e.g., [13], with a model of nozzle flow upstream of separation. See Fig. 9 in [12]. The second uses scaling to obtain an approximate model of mean separation line motion as a function of time (altitude). This approach will be described in a future paper.

- B) The parameter $\Delta P(t) = P_i(t) - P_a(t)$, requires estimation of $P_i(t)$, the nozzle-wall pressure near the incipient separation point. Again, an alternative to complex modeling and numerics can be found in a semi-empirical approach outlined in [12].
- C) Examination of the working formulae used to compute theoretical variances (see Appendix A) shows that the three *a priori* unknown boundary layer parameters, σ_s , ϵ , and τ_c , representing, respectively, the nominal length of the boundary layer-shock interaction zone ($\sigma_s \approx L_s$), the ratio of the boundary layer to rocket dynamics time scales, and the correlation time for local separation line displacements, *only* appear as the product, $\kappa_o = \sigma^2 \tau_c \epsilon$. Thus, Model II has only *one* available adjustable parameter, κ_o , for fitting theoretical to experimental data.
- D) Rather than employing any of a number of standard fitting procedures for estimating κ_o , we use the following simple approach. First, express κ_o as $\kappa_o = \beta_o \sigma_o^2 \epsilon_o \tau_{co}$, where β_o becomes the fitting parameter and the last three parameters are assigned nominal, empirically- or scaling-based values: $\sigma_o = 2.54 (10^{-2})$ m [13,31], $\epsilon = 0.1$ (scaling), and $\tau_c = 10^{-3}$ s [31,32]. Second, use straightforward trial and error to estimate β_o . Since the β_o thus obtained is nearly equal

to $1/4$, we arbitrarily set $\beta_o = 0.25$.

- E) It is important to note that if we reasonably (though arbitrarily) take τ_c as the most uncertain of the three parameters σ , ϵ , and τ_c , i.e., express τ_c as $\tau_c = \beta_o \tau_{co}$, and interpret τ_c as the approximate frequency of large-scale separation line motion [34], then the *estimated* value of $\tau_c^{-1} = 400$ Hz, is comparable to frequencies (≈ 300 Hz) experimentally observed in shock-separated flat plate boundary layers [31].
- F) As noted in Appendix A, scaling, as well as numerical results (Model I), show that during the side load period, $0 \leq t < T$, variance growth in lateral rocket displacements, $Y_o(t)$ and $Z_o(t)$, remains negligible relative to that observed during the post-side-load period, $T < t \leq T_f$. For simplicity, during $0 \leq t < T$, theoretical (Model II) displacement variances are thus set to 0.
- G) Parameters defining the model rocket can be found in [11].
- H) An ensemble of 100 numerically simulated rocket ascents are used to estimate experimental (Model I) means and variances. Since time-dependent statistics estimated using a smaller set of 40 ascents differed by no more than 14 % from these, no attempt has been made to examine larger ensembles.
- I) As noted in section 6, theoretical time evolution of the following *mean* values: pitch and yaw rate, $\langle \omega_z(t) \rangle$ and $\langle \omega_y(t) \rangle$, pitch and yaw displacement, $\langle \theta(t) \rangle$ and $\langle \psi(t) \rangle$, lateral velocity, $\langle \dot{Y}_o \rangle$ and $\langle \dot{Z}_o \rangle$, and lateral displacement, $\langle Y_o(t) \rangle$ and $\langle Z_o(t) \rangle$, all remain identically zero throughout the simulated flight period, $0 \leq t \leq T_f$. These results are, in every instance, consistent with the numerical observations in [11].

In discussing the results, we follow three threads:

- A) Evolution of pitch and yaw *rate* variances turn out to play a central role in evolution of not only pitch and yaw *displacement* variances, but also in variance evolution of lateral translational velocities and displacements. In the latter cases, *thrust components* produced by random pitch and yaw emerge as the dominant mechanism generating translational stochasticity.
- B) We find that physical interpretation of many of the results below can be usefully framed in terms of the OU damping and diffusion coefficients, $A(t)$ and $D(t)$, given respectively by (29) and (32). The utility of these parameters traces to the central role played by random pitch and yaw rates in stochastic rocket dynamics.
- C) The transparent physical content of $A(t)$ and $D(t)$ allows straightforward identification of practical approaches for minimizing or mitigating against the effects random pitch and yaw.

7.1. Pitch and yaw rate response

Numerical and theoretical pitch and yaw rate variances, $\langle \omega_z^2(t) \rangle$ and $\langle \omega_y^2(t) \rangle$, are compared in Fig. 5. General theoretical expressions, applicable over the side load period and post load period, are given respectively by Eqs. (37) and (41); corresponding expressions specific to the present model are given by (A-1) and (A-3). It is clear that theoretical pitch and yaw rate variances remain qualitatively consistent with numerical estimates throughout the entire flight period.

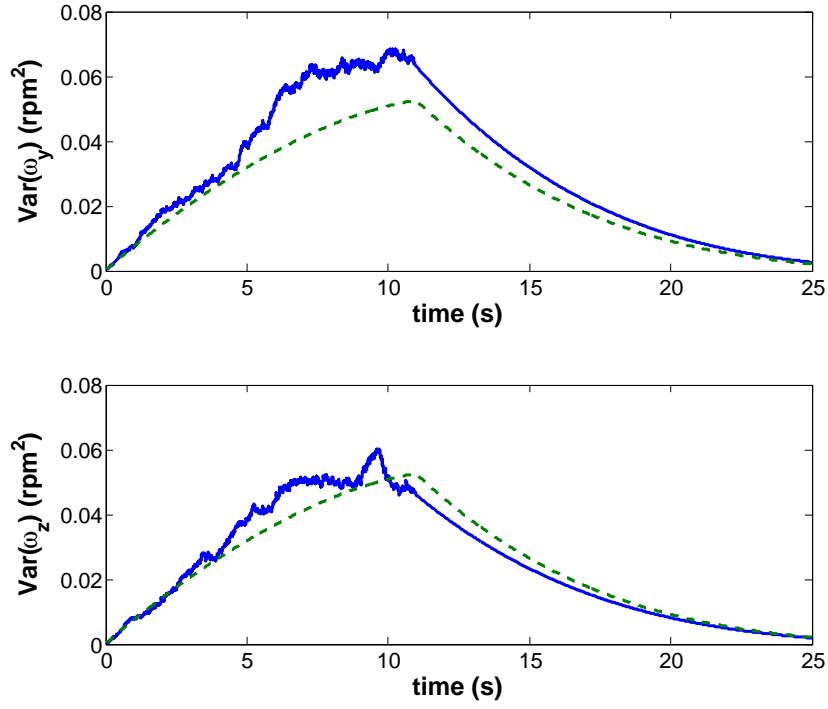


Figure 5: Comparison of yaw, ω_y , and pitch, ω_z , rate variance evolution as estimated using Model I (solid line) and as computed via Model II (dashed line). The side load period ends at $t = 10.85$ s.

7.1.1. Pitch and yaw rate response: side load period

During the side load period, theoretical and numerically observed stochasticity, indicated by the variances, clearly increase in a qualitatively consistent manner. [Note, differences between ensemble-averaged pitch and yaw rate variances decrease when the ensemble is enlarged from 40 to 100 simulated flights. We anticipate that the observed differences in figure 5 become negligible, as they should by symmetry, as $N \rightarrow \infty$. A similar comment applies to all other numerical results.]

Physical insight into variance growth during the side load period, and identification of design approaches for minimizing growth of stochastic pitch and yaw, follows by looking at a simpler model. Thus, take the damping and diffusion coefficients, $A(t)$ and $D(t)$, in (29) and (32), as constant. Although an approximation here, this simplification becomes increasingly accurate as the side load period shortens. Under this approximation, variance growth follows the standard OU formula [39]:

$$\langle \omega_\alpha^2(t) \rangle = \frac{D_o}{2A_o} (1 - \exp(-2A_o t)) \quad (75)$$

with the associated rate of variance growth, valid in the limit $A_o T \ll 1$, given by

$$\frac{d \langle \omega_\alpha^2(t) \rangle}{dt} = D_o + O(A_o T) \quad (76)$$

Here, $A_o = A(0)$ and $D_o = D(0)$.

We use (75) to examine physical features underlying pitch/yaw rate variance in the limit, $A_o T \gg 1$, appropriate under conditions where damping is strong and/or ascent is slow. Equation (76) is used to examine the opposite limit, $A_o T \ll 1$, i.e., the limit applicable to the present

numerical [11] and theoretical models.

Considering first $A_o T \gg 1$, the asymptotic variance takes the form:

$$\langle \omega_\alpha^2(t) \rangle \approx \frac{D_o}{2A_o} \approx \frac{R^2(0)\Delta^2 P(0)\pi\sigma^2\epsilon}{I(0)|\dot{M}|} \quad (77)$$

where, as determined by scaling, the relationships, $|\dot{M}|(L-b)^2 \gg \dot{I}$ and $|\dot{M}|(L-b)^2 \gg 0.25R_e^2$, have been used; refer to (29).

Physically, the right side of (77) represents the ratio of stochasticity *amplification* via side-load-induced random torques, to stochasticity *stabilization* via mass flux damping. The former feature becomes apparent when we restore the squared moment arm, $(L-b)^2$, cancelled in obtaining (77).

The role of mass flux damping can be ascertained by sketching the incremental (vector) change, $\Delta\dot{\mathbf{M}}$, in the mass flux vector, $\dot{\mathbf{M}}$, produced by an incremental pitching or yawing displacement (about the pitch or yaw axis). Such a sketch shows that $\Delta\dot{\mathbf{M}}$ acts (nominally) in the plane of the nozzle exit, in a direction opposing the angular motion. Thus, with reference to (29), (33), and (34), we recognize that $\Delta\dot{\mathbf{M}}$ produces a retarding, i.e., stabilizing torque that opposes *all* pitch and yaw motions.

Based on this interpretation, we can use (77) to identify practical approaches, appropriate when $A_o T \gg 1$, for either reducing random pitch/yaw amplification, or increasing mass flux damping:

- a) reduce the nozzle size (characterized by $R(0)$),
- b) reduce the near-exit, ground-level pressure difference, $\Delta P(0)$, e.g., by reducing the degree of over-expansion,

c) increase the rocket's moment of inertia, as characterized by $I(0)$, and/or

d) increase the mass flux, \dot{m} .

These observations presume, reasonably, that the boundary layer separation parameters, σ_s , τ_c , and ϵ remain, in an order of magnitude sense, independent of nozzle size and in-nozzle flow conditions.

Turning to the limit where the side load period is too short for the asymptotic regime to set in, $A_o T \ll 1$, again the limit appropriate to the present study and that in [11], we expose features that determine the *rate* of variance growth. Again using initial values for the parameters in (32), Eq. (76) yields (to $O(A_o T)$)

$$\begin{aligned} \frac{d \langle \omega_\alpha^2(t) \rangle}{dt} &= D_o \\ &= (L - b)^2 I^{-2}(0) R^2(0) \Delta^2 P(0) 2\pi \sigma_s^2 \tau_c \epsilon \end{aligned} \tag{78}$$

Again assuming that the parameters σ_s , τ_c , and ϵ remain nominally independent of nozzle size and in-flight nozzle flow conditions, we observe that the rate of pitch/yaw rate variance growth can be minimized, e.g., by:

a) again using high-rotational inertia rocket designs,

b) moving the center of mass toward the nozzle exit (thus reducing the moment arm, $L - b$),
while maintaining high I ,

c) using smaller (radius) nozzles, and of course when feasible,

d) operating in an underexpanded condition,

where d) eliminates separation and thus side loading.

Other approaches, designed to reduce σ_s , τ_c , and/or ϵ , might include boundary layer manipulation via, e.g., wall fluid injection or suction, and/or active or passive mechanical forcing.

7.1.2. Pitch and yaw rate response: post-side-load period

Side loads cease when the rocket reaches an altitude where ambient pressure drops below the near-exit nozzle pressure. From this instant onward, and as is apparent in both numerical and theoretical plots of $\langle \omega_\alpha^2 \rangle$ in Fig. 5, rocket pitch and yaw, become subject only to the damping torque produced by incremental changes in $\dot{\mathbf{M}}$.

Equation (41) shows that the post-side-load decay in pitch/yaw rate variance is exponential, with the rate of damping increasing with time. Physically, and as shown by (29), accelerated rotational damping, in turn, reflects the inverse dependence of the damping coefficient, $A(t)$, on the time-decaying moment of inertia, $I(t)$: as the rocket becomes decreasingly resistant to pitch/yaw rotations, the damping torque can effect ever-larger influence on pitch and yaw.

We can use (29) to quickly identify design strategies that, e.g., enhance post-side-load damping of random pitch and yaw. Thus, assuming that the term in R_e^2 is small, the case here, then

a) increasing \dot{M} , and/or

b) increasing the moment arm, $L - b$,

will improve damping.

Clearly, trade-offs are required since, for example, strategy b) *enhances* variance growth during the side load period. By contrast, increasing nozzle mass flux, at least up to magnitudes for which $|\dot{I}|$ remains smaller than $|\dot{M}|(L - b)^2$, is always beneficial since this enhances mass-flux damping. [Interestingly, for large enough $|\dot{M}|$, the negative term, \dot{I} , in (29) can become dominant, transforming $A(t)$ into an *amplification* coefficient. A simple analog that explains this effect can be found in the gravity-driven pendulum: shortening the pendulum length during motion increases the amplitude of the motion.]

7.2. Pitch/yaw displacement variance

Pitch and yaw displacement variances are compared in Fig. 6. General theoretical expressions for the side load and post side load periods are given respectively by Eqs. (49) and (53), and problem-specific versions are derived in Appendix A. As in the case of pitch/yaw rate variances, reasonable consistency between theoretical and numerical results is again observed.

In order to interpret variance growth during the side load period, we again note that due to the brevity of the side load period, $A(t)$ and $D(t)$ can be approximated as constant and equal to, say, $A_o = A(0)$ and $D_o = D(0)$. Starting with (49), noting that $A_o T \ll 1$, and expanding (49) in $A_o t$ then leads to

$$\langle \psi_\alpha^2(t) \rangle \approx \frac{D_o}{3} t^3 + O(A_o^4 t^4)$$

where $1 \gg \frac{D_o}{3} t^3 \gg A_o^4 t^4$, and where D_o is given by (78). Thus, the observed growth in pitch/yaw variance during side loading reflects the dominant effect of *diffusive*, i.e., stochastic, side-load-driven growth over mass-flux damping. Variance growth is slow since the diffusion coefficient, D_o , is small;

a quick order of magnitude estimate, yielding $D_o \approx 10^{-5} \text{ s}^{-3}$, shows that $D_o t^3/3$ is on the order of observed and predicted side load period variances.

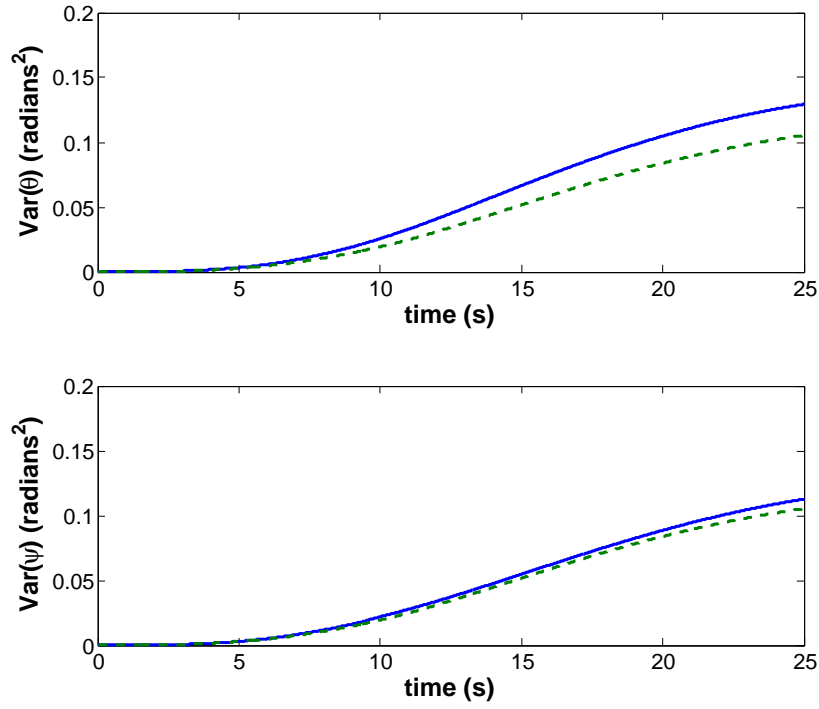


Figure 6: Comparison of pitch, θ , and yaw, ψ , displacement variance evolution as estimated using Model I (solid line) and as computed via Model II (dashed line). The side load period ends at $t = 10.85$ s.

During the post-side-load period, and based on (50), it proves useful to interpret the term, $\int_T^t h(s')ds'$, appearing in (53) as a response function; here, the function yields the total random change in pitch/yaw displacement, over the interval from T to t , produced by the random initial pitch/yaw rate, $\omega_\alpha(T)$. Thus, examining the three terms on the right side of (53), we observe that the displacement variance at t , $\langle \psi_\alpha^2(t) \rangle$, corresponds to the sum of: i) the average squared response to the random input $\omega_\alpha(T)$, ii) the *weighted* average *linear* response to $\omega_\alpha(T)$, where weighting is with respect to the random initial displacement, $\psi_\alpha(T)$, and iii) the initial displacement variance, $\langle \psi_\alpha^2(T) \rangle$. While the response function increases with time, $t - T$, it is readily shown that the rate of increase decays with increasing $t - T$; thus, in Fig. 6, we observe a roll-off in displacement variance.

It now becomes apparent that post-side-load displacement variance at any time t increases (decreases) with any increase (decrease) in any of the above inputs. This picture provides an explanation, for example, of the larger post-side-load *numerical* (Model I) yaw variances observed in Fig. 6. As another example, under circumstances where damping, $A(t)$, decreases, we expect, based on simple physical intuition, that the lag between angular velocities and displacements decreases and thus, the correlation $\langle \omega_\alpha(T)\psi_\alpha(T) \rangle$, increases. Thus, consistent with our intuition, weakly damped rockets arrive at $t = T$ with a greater range of random pitch/yaw displacements; this initial input, in turn, leads, via the response function, to larger post-side-load displacement variance. Clearly, practical design considerations, similar to those discussed above, can be identified and used to manipulate the response function.

7.3. Lateral velocity and displacement variance

Lateral velocity and displacement variances obtained via Models I and II are compared in Figs. 7 and 8, respectively. Full theoretical velocity expressions applicable to the side load and post side load periods are given respectively by Eqs. (69) and (70). Corresponding expressions for theoretical displacement variances are given in (73) and (74).

The most important observation, as mentioned above and as discussed in Appendix A, concerns the post-side-load emergence of the thrust force term: as shown by Eqs. (A-10) and (A-13), post-side-load lateral velocity and displacement variances are overwhelmingly determined by the thrust force component acting in the random pitch and yaw directions.

Insight into variance growth over the entire flight period can be gained by interpreting and scaling individual terms contributing to the velocity variance in (69) and (70). Thus, taking the side load period first, the terms on the right side of (69) correspond, respectively, to velocity *variance-production* via: i) weak random side loads (weak relative to the thrust, F_T), ii) translational reaction to weak mass flux damping of random pitch and yaw rates, iii) laterally-acting components of the thrust force, and iv) coupling of effects ii) and iii). While F_T is large, angular displacements during $0 \leq t < T$, relative to those appearing during the post-side-load period, remain small.

During the post-side-load period, the side load contribution, i), drops out and a contribution, $< \dot{\eta}^2(T) >$, capturing the lumped, integrated effects of ii) through iv), replaces it. During this period, angular displacements grow large enough for large lateral thrust force components to appear, generating, in turn, large lateral velocities and displacements.

Notice that lateral displacements, on the order of several kilometers, are observed. As discussed

in [11], scaling readily shows that experimental and theoretical displacements are consistent with the magnitudes of computed side loads, thrust forces and angular displacements. Note too, that these displacements represent small fractions of the rocket's vertical displacement; the difference

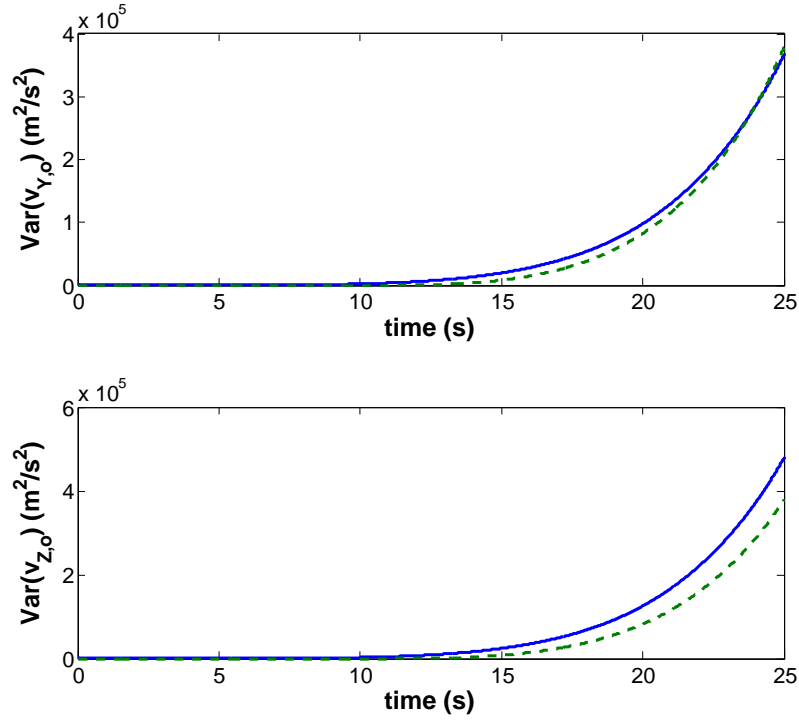


Figure 7: Comparison of lateral rocket velocity variance evolution as estimated using Model I (solid line) and as computed via Model II (dashed line). The side load period ends at $t = 10.85$ s.

between ideal, zero-side-load three-dimensional rocket displacements (relative to the launch location) and displacements observed when side loads are accounted for, remains less than 0.1 % over the simulated flight period, $(0, T_f]$ [11].

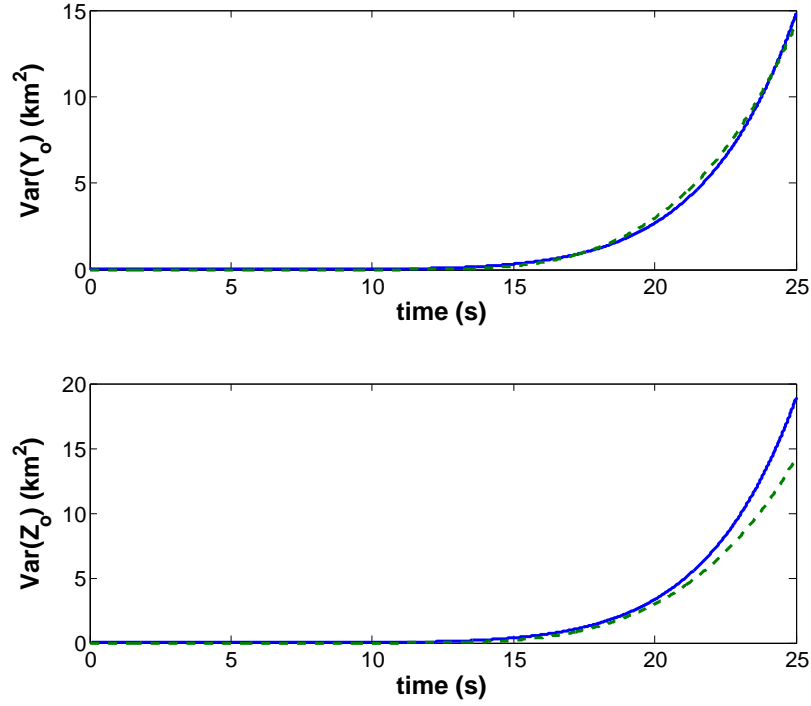


Figure 8: Comparison of lateral rocket displacement variance evolution as estimated using Model I (solid line) and as computed via Model II (dashed line). The side load period ends at $t = 10.85$ s.

8. Summary and conclusions

A set of analytical models are proposed which connect stochastic, shock-induced boundary layer separation in over-expanded nozzles, to random nozzle side loads and associated rocket response. The broad objectives center on establishing the consistency of Models I [11] and II, and on broadening understanding of the physical features connecting boundary layer separation and rocket response.

The physical consistency of Model I is established by demonstrating that the simple model of stochastic separation line evolution proposed in [11] allows direct *derivation* of the *ad hoc* side load model assumed in [11], as well as derivation of observed side load amplitude and direction probability densities [18–20]; the demonstration thus ties the most uncertain elements of Model I, the separation line and side load models, to experimental observation. The consistency of the analytical models proposed here, collectively Model II, is established by showing that predicted altitude-dependent statistics of rocket rotational and translational motion are, in every case examined, consistent with those predicted by Model I.

From a practical standpoint, the analytical models proposed here provide a simple framework for analyzing stochastic rocket response to side loading, as well as identifying design strategies that minimize either side loads, side load-induced torques, and/or rocket response to these loads and torques.

Appendix A: problem-specific variances

Detailed variance expressions for pitch and yaw rates and angles, and lateral translational velocities and displacements, appropriate to the set of conditions used in numerical experiments, are given

here. A few non-trivial derivational details are included.

Variances during the side load period, $0 \leq t < T$, depend on the diffusion coefficient, $D(t)$, and damping coefficient, $A(t)$, given respectively by Eqs. (32) and (29). These in turn depend on the time dependent position of the shock in the nozzle, $x_s(t)$ (as given implicitly by $R(t)$), the time-dependent pressure difference, $\Delta P(t)$, the time-dependent rocket mass, $M(t)$, and moment of inertia, $I(t)$. Here, these terms are determined via quadratic fits to data from numerical experiments; under, e.g., real flight conditions, these terms could, in principal, be estimated using computational fluid dynamics simulations, perhaps combined with experimental measurements.

Pitch and yaw rate variances

Pitch and yaw rate variances during the side load period, given by Eq. (37), assume the specific form:

$$\langle \omega_\alpha^2(t) \rangle = (L - b)^2 2\pi \sigma_s^2 \tau_c \epsilon \left[\frac{I_o - |\dot{I}|t}{I_o} \right]^{c_1} \int_0^t \frac{R^2(s') \Delta^2 P(s')}{I^2(s')} \left[\frac{I_o}{I_o - |\dot{I}|s'} \right]^{c_1} ds' \quad 0 \leq t \leq T \quad (\text{A-1})$$

where

$$c_1 = 2 \left[\frac{\dot{I} + |\dot{M}|(L - b)^2}{|\dot{I}|} \right] \quad (\text{A-2})$$

and where, due to the fixed magnitude of \dot{M} ,

$$M(t) = M_o - |\dot{M}|t$$

$$I(t) = I_o - |\dot{I}|t$$

Derivation of (A-1) is straightforward, requiring separate evaluation of the three integrals in (37), with, e.g., the equation immediately above used for the $I(t)$ term in the diffusivity, $D(t)$ (equation (32)), and by noting throughout that \dot{M} and \dot{I} are constant.

During the post-side-load period, $T < t \leq T_f$, Eq. (41) assumes the specific form:

$$\langle \omega_\alpha^2(t) \rangle = \langle \omega_\alpha^2(T) \rangle \left[\frac{I_o - |\dot{I}|t}{I_o - |\dot{I}|T} \right]^{c_1} \quad T < t \leq T_f \quad (\text{A-3})$$

Pitch and yaw variances

The general forms of the side-load-period and post-side-load pitch/yaw variances are given respectively by (49) and (53). The former takes the specific form

$$\langle \psi_\alpha^2(t) \rangle = 2 \int_0^t \left[\frac{I_o - |\dot{I}|q'}{I_o} \right]^{c_1/2} \left(\int_0^{q'} F_1(q) \left[\frac{I_o - |\dot{I}|q}{I_o} \right]^{c_1/2} dq \right) dq' \quad 0 \leq t < T \quad (\text{A-4})$$

where

$$F_1(q) = 2\pi\sigma_2^2\tau_c\epsilon(L-b)^2 \int_0^q \frac{R^2(s')\Delta^2 P(s')}{I^2(s')} \left[\frac{I_o}{I_o - |\dot{I}|s'} \right]^{c_1} ds' \quad (\text{A-5})$$

Again, this expression follows via straightforward evaluation and integration of individual terms in (49).

Pitch/yaw variance during the post-side-load period is most easily determined by computing individual terms in (53). Thus,

$$\langle \omega^2(T) \rangle \left(\int_T^t h(s') ds' \right)^2 = \frac{\langle \omega^2(T) \rangle}{(I_o - |\dot{I}|T)^{c_1}} \frac{1}{|\dot{I}|(1+c_2)} \left[(I_o - |\dot{I}|T)^{c_2+1} - (I_o - |\dot{I}|t)^{c_2+1} \right] \quad (\text{A-6})$$

where $c_2 = c_1/2 = \left(\dot{I} + |\dot{M}|(L - b)^2 \right) / |\dot{I}|$. In addition,

$$2 \langle \omega_\alpha(T) \psi_\alpha(T) \rangle \left(\int_T^t h(s') ds' \right) = 2 \langle \omega_\alpha(T) \psi_\alpha(T) \rangle \frac{1}{(I_o - |\dot{I}|T)^{c_2}} \frac{1}{|\dot{I}|(1 + c_2)} \left[(I_o - |\dot{I}|T)^{c_2+1} - (I_o - |\dot{I}|t)^{c_2+1} \right] \quad (\text{A-7})$$

where the detailed form of $\langle \omega_\alpha(T) \psi_\alpha(T) \rangle$ follows from (56):

$$\langle \omega_\alpha(T) \psi_\alpha(T) \rangle = \int_0^T \left[\frac{I_o - |\dot{I}|q}{I_o} \right]^{c_2} \left[\frac{I_o - |\dot{I}|T}{I_o} \right]^{c_2} \int_0^q D(s') g^2(s') ds' dq \quad (\text{A-8})$$

and where, from (32) and the definition of g immediately following (56)

$$D(s') g^2(s') = 2\pi \sigma_s^2 \tau_c \epsilon (L - b)^2 \left(\frac{R^2(s') \Delta^2 P(s')}{I^2(s')} \right) \left[\frac{I_o}{I_o - |\dot{I}|s'} \right]^{c_1} \quad (\text{A-9})$$

The final term in (53), $\langle \psi_\alpha^2(T) \rangle$, follows by setting $t = T$ in (A-4).

Lateral translational velocity and displacement variances

Full expressions for lateral translational velocity variances during and subsequent to the side load period are given respectively by (69) and (70). Corresponding displacement variances are given by (73) and (74). Considering the entire flight period, $0 \leq t \leq T_f$, we find via scaling and numerical experiments that in the present model, velocity and displacement variances remain small during the side load period, but grow explosively during the post-side-load period.

Due to the dominance of post-side-load variances, for simplicity, and as mentioned, when computing theoretical velocity and displacement variances, we simply compute $\langle \dot{\eta}^2(t) \rangle$ and $\langle \eta^2(t) \rangle$

during the post-side-load period, using only the terms involving the thrust force, F_T . It is readily shown that these terms are, at minimum, two orders of magnitude larger than all other, neglected terms.

Thus, the post-side-load velocity variance assumes the form:

$$\langle \dot{\eta}^2(t) \rangle = \int_T^t \int_T^t \frac{F_T(s')F_T(p')}{M(s')M(p')} \langle \psi_{\alpha\pm}(s')\psi_{\alpha\pm}(p') \rangle ds' dp' \quad (\text{A-10})$$

The time correlation function, in turn, is given as the weighted sum of three separate variances:

$$\langle \psi_{\alpha\pm}(s')\psi_{\alpha\pm}(p') \rangle = k(s')k(p') \langle \omega_{\alpha\pm}^2(T) \rangle + \langle \psi_{\alpha\pm}^2(T) \rangle + [k(s') + k(p')] \langle \omega_{\alpha\pm}(T)\psi_{\alpha\pm}(T) \rangle \quad (\text{A-11})$$

where

$$k(q) = \frac{1}{(I_o - |\dot{I}|T)^{c_2}} \frac{1}{|\dot{I}|(1 + c_2)} \left[(I_o - |\dot{I}|T)^{c_2+1} - (I_o - |\dot{I}|q)^{c_2+1} \right] \quad (\text{A-12})$$

The term $\langle \omega_{\alpha\pm}^2(T) \rangle$ follows by using $t = T$ in (A-1), $\langle \psi_{\alpha\pm}^2(T) \rangle$, follows by doing the same in (A-4), and $\langle \omega_{\alpha\pm}(T)\psi_{\alpha\pm}(T) \rangle$ is given by (A-8).

Finally, lateral displacement variance during the post-side-load period is given by

$$\langle \eta^2(t) \rangle = \int_T^t \int_T^t \langle \tilde{F}(s')\tilde{F}(p') \rangle ds' dp' \quad (\text{A-13})$$

where

$$\langle \tilde{F}(q)\tilde{F}(q') \rangle = \int_T^{q'} \int_T^q \frac{F_T(s')F_T(s)}{M(s')M(s)} \langle \psi_{\alpha\pm}(s')\psi_{\alpha\pm}(s) \rangle ds' ds \quad (\text{A-14})$$

Appendix B: Random wind effects

When considering the dynamic effects of wind loading, it is useful to focus on the ratio of the characteristic time scale associated with say a turbulent cross-wind, $\tau_w = l_w/v_w$, relative to the rocket dynamics time scale, $\tau_R = L_R/V_R$:

$$\frac{\tau_w}{\tau_R} = \frac{l_w}{L_R} \frac{V_R}{v_w} \quad (\text{B-1})$$

where l_w and v_w are the integral length and velocity scales for the cross-wind, L_R is the rocket length, and V_R is the characteristic rocket speed. Given reasonable, readily estimated velocity scales, then wind loading produces non-negligible pitch and yaw responses only under conditions where the length scale ratio produces time scale ratios of order one or less. Under these circumstances, the turbulent wind loads act fast enough to produce non-negligible pitch and yaw moments. In contrast, when the turbulence time scale is much larger than the rocket dynamics time scale, then lateral wind turbulence merely produces random lateral displacements, with minimal pitch and yaw (where the random translational response presumably has zero mean relative to the mean displacements and velocities produced by the mean cross-wind).

Based, e.g., on a large number of altitude-dependent wind measurements (taken under nominally normal daytime conditions at Cape Kennedy) [40], $v_w = O(10 \text{ m/s})$, while $l_w = O(10^3 \text{ m})$, where the latter corresponds to the approximate correlation length scale. Thus, since $V_R = O(10^3 \text{ m/s})$ and $L_R = 10 \text{ m}$, $\tau_w/\tau_R = O(10^4)$. While prevailing winds thus have negligible effect on representative rocket rotational dynamics, the wind nevertheless produces a random, translational response.

Indeed, a quick estimate shows that the lateral wind load ($= O(\rho_a \bar{V}_w^2 A_R)$, where A_R is the rocket lateral area) is of the same order as the characteristic side load (estimated below); however, since the side load time scale is fast, specifically, faster than the rocket time scale, τ_R , then the slow-time scale dynamics produced by wind can be neglected when studying the response produced by side loads. [When computing the combined effect of random wind and side loading, due to the separation in response time scales, the response to the former can be simply superposed on that produced by the latter.]

References

- [1] M. Gruntman, *Blazing The Trail: The Early History Of Spacecraft and Rocketry* (AIAA, Reston, VA, 2004), Chap. 1.
- [2] G. P. Sutton and O. Biblarz, *Rocket Propulsion Elements, 7th ed.* (Wiley, New York, 2001), pp. 104-106.
- [3] F. B. Leahy, "Discrete gust model for launch vehicle assessemnts," presented at the 12th Conf. on Aviation, Range and Aerospace Metrology (Jan. 2008).
- [4] E. L. Flemming, S. Chandra, M. R. Schoeberl, and J. J. Barnett, NASA TM-100697 (1988).
- [5] C. G. Justus and D. L. Johnson NASA TM-1999-209630 (1999).
- [6] C. G. Justus, C. W. Campbell, M. K. Doubleday, and D. L. Johnson, NASA TM 4168 (1990).
- [7] R. H. Schmucker, NASA Rep. 77396 (1984).

- [8] H. N. Abramson, R. J. Martin, and G. E. Ransleben, Jr., Southwest Research Institute Technical Report No. 1 (1958).
- [9] H. J. Buchanan and F. M. Bugg, NASA TN D-3968 (1967).
- [10] I. I. McNaughtan, Aircraft Engrg. Aerospace Tech. **36**, 409 (1993).
- [11] N. Srivastava, P. T. Tkacik, and R. G. Keanini, J. Appl. Phys. **108**, 044911 (2010).
- [12] R. G. Keanini and A. Brown, Eur. J. Mech. B - Fluids **26**, 494 (2007).
- [13] J. Ostlund, Ph.D. Thesis, Royal Inst. Tech., 2002.
- [14] J. Ostlund, T. Damgaard, and M. Frey, AIAA J. Propulsion and Power **20**, 695 (2004).
- [15] M. Frey and G. Hagemann, AIAA Paper 98-3619 (1998).
- [16] T. A. de Roquefort, in *Proceedings of the Fourth European Symposium on Aerothermodynamics for Space Applications*, (Capua, Italy, 2002), p. 93.
- [17] G. E. Dumnov, AIAA Paper 96-3220 (1996).
- [18] S. Deck and A. T. Nguyen, AIAA J. **42**, 1878 (2004).
- [19] S. Deck, E. Garnier, and P. Guillen, J. Turbulence **3**, 1 (2002).
- [20] S. Deck and E. Garnier, in *Proceedings of the Fifth European Symposium on Aerothermodynamics for Space Vehicles*, edited by D. Danesy (Cologne, Germany, 2004), p. 297.

- [21] C. Hagemann, M. Terhardt, M. Frey, P. Reijasse, M. Onofri, F. Nasuti, and J. Ostlund, in *Proceedings of the Fourth International Symposium on Liquid Space Propulsion*, (German Aerospace Center, Lampoldshausen, 2000).
- [22] L. H. Nave and G. A. Coffey AIAA Paper 73-1284 (1973).
- [23] J. Ostlund and B. Muhammad-Klingmann, Appl. Mech. Rev. **58**, 143 (2005).
- [24] M. Frey and G. Hagemann, J. Propul. Power **16**, 478 (2000).
- [25] F. Onofri and M. Nasuti, AIAA Paper 99-2587 (1999).
- [26] L.-O. Pekkari, AIAA Paper 94-3377 (1994).
- [27] R. Schwane and Y. Xia, J. Math Model Algorithms **4**, 53 (2005).
- [28] T. Shimizu, M. Kodera, and N. Tsuboi, J. of the Earth Simulator **9**, 19 (2008).
- [29] G. Settles, I. E. Vas, and S. M. Bogdonoff, AIAA Journal **14**, 1709 (1976).
- [30] G. Settles, W. Fitzpatrick, and Bogdonoff, S., AIAA Journal **17**, 579 (1979).
- [31] D. S. Dolling and L. Brusniak, AIAA J. **27**, 734 (1988).
- [32] M. E. Erengil, Ph.D. Thesis, University of Texas, Austin, 1993.
- [33] H. W. Liepmann, A. Roshko, and S. Dhawan, NACA Report 1100 (1952).
- [34] M. E. Erengil and D. S. Dolling, AIAA J. **29**, 1868 (1990).
- [35] R. Sekita, A. Watanabe, K. Hirata and T. Imoto, Acta Astronautica **48**, 431 (2001).

- [36] T. Tran and F. O. Eke, Adv. Astronaut. Sci. **119**, 1297 (2004).
- [37] C. T. Force, ARS J. **32**, 1095 (1962).
- [38] K. J. Plotkin, AIAA J. **13**, 1036 (1975).
- [39] C. Gardiner, *Stochastic Methods: A Handbook for the Natural and Social Sciences, Third ed.*
(Springer-Verlag, Berlin, 2004), p. 74.
- [40] M. E. White, *Wind Loads During Ascent*, NASA SP-8035 (1970).